Lithos 376–377 (2020) 105748

Contents lists available at ScienceDirect

Lithos

journal homepage: www.elsevier.com/locate/lithos

Research Article

Subduction initiation of Proto-Tethys Ocean and back-arc extension in the northern Altun Mountains, northwestern China: Evidence from high-Mg diorites and A-type rhyolites

Xian-Tao Ye [a,b,*], Chuan-Lin Zhang [a], Qian Wang [a], Guo-Dong Wang [c]

[a] C llege f Ocea g a h , H hai U i e i , Na ji g 210098, Chi a

[b]

-0.78). Thei ele e al g e che i a d c led ega i e h le- ck ε

Nd(

(480-495 M
rollback of
~460 Ma ar
as well as T
ern Gondwa

1. I d c

Subduction initiation and back-arc extension are important tectonic processes, and are generally associated with negative buoyancy of oceanic lithosphere (Crameri et al., 2020; Stern and Gerya, 2018; Tontini et al., 2019) and trench retreat (Gueydan et al., 2017; Magni et al., 2017), respectively. The timing of subduction initiation and identification of arc and back-arc systems can therefore provide critical information for paleo-subduction zone development (e.g. Chen et al., 2014; Keenan et al., 2016; Song et al., 2013; Xia et al., 2012). In addition, subduction initiation can induce partial melting of the oceanic slab and overlying sediments, leading to the formation of adakitic rocks and high-Mg andesites (Defant and Drummond, 1990; Peacock, 1990). Asthenospheric upwelling caused by slab rollback can produce a wide variety of magmatic rocks (e.g. adakites, mafic dykes and high-Mg andesites), and may also cause a back-arc extension, resulting in the

* Corresponding author at: College of Oceanography, Hohai University, Nanjing 210098, China.
E- ail add e : yexiantao10@mails.ucas.ac.cn (X.-T. Ye).

https://doi.org/10.1016/j.lithos.2020.105748

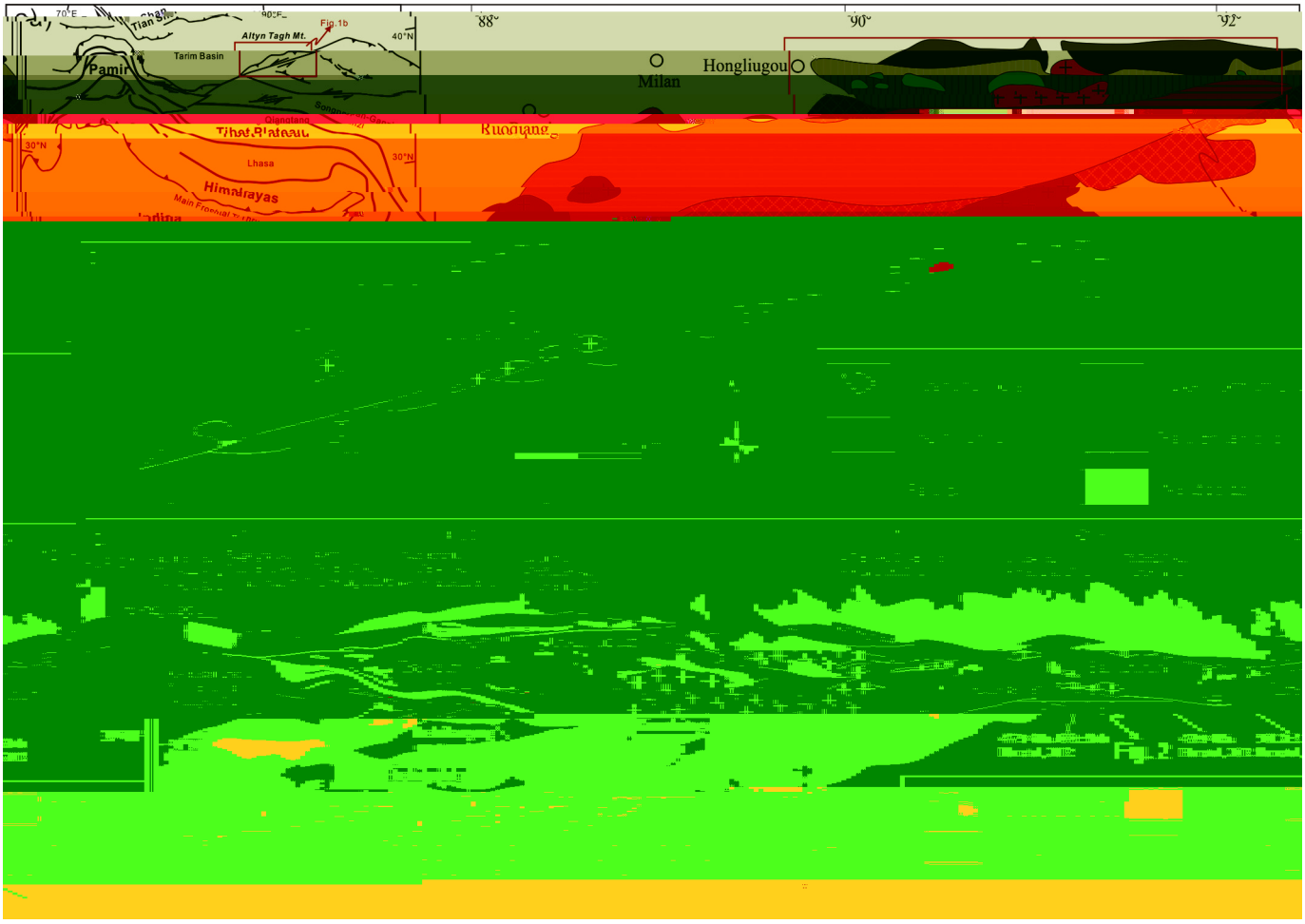

F g. 1. (a) Simplified tectonic map of the Indo-Asian collision zone showing major active structures and suture zones (modified after Yin and Harrison, 2000); (b) Geologic and tectonic map of the Altun orogen; (c) Geologic map of the North Altun Orogenic Belt (modified after Liu et al., 2017).

generation of back-arc basin basalts (BABB) and A-type granitoids (Ewart et al., 1998; Shinjo et al., 1999; Sibuet et al., 1987).

The Proto-Tethys Ocean opened during the late Neoproterozoic due to the breakup of Rodinia and mainly closed at the end of the early Silurian (Li et al., 2018a; Matte et al., 1996). A better understanding of the evolution of the Proto-Tethys Ocean is important for reconstructing the East Asia continents in Proto-Tethys realm. Based on the age of ophiolite complex and rift-related volcanism, recent studies indicated that the Proto-Tethys Ocean in Qingling-Qilian-Kunlun was developed in the Late Neoproterozoic (~600-580 Ma) (Dong et al., 2011; Song et al., 2013; Xu et al., 2015), subducted at ~520 Ma (Chen et al., 2014; Liu et al., 2016a; Meng et al., 2017; Song et al., 2013; Xia et al., 2012) and closed at ~440-430 Ma (Song et al., 2014, 2018; Yang et al., 2018; Zhang et al., 2013).

The North Altun Orogenic Belt (NAOB) is one of the key tectonic units of the Altun Orogen which is an important segment of the Qinling-Qilian-Kunlun orogenic system. As the northernmost orogenic collage of the Proto-Tethys domain, the NAOB is a well-preserved early Paleozoic trench–arc–basin system (Zhang et al., 2017) that is critical for the understanding of the Proto-Tethys Ocean evolution (Li et al., 2018a). Although the tectonic evolution of the NAOB is divided into three stages and it is known that subduction of oceanic slab occurred during 520–460 Ma (Han et al., 2012; Liu et al., 2016b; Meng et al., 2017; Wu et al., 2009; Ye et al., 2018; Zheng et al., 2019), the subduction history remains enigmatic. In particular, the timing of initial subduction and back-arc extension in NAOB is poorly constrained.

Here we present detailed field observations, ages, and geochemistry for newly identified high-Mg diorites and A-type rhyolites in the central NAOB. We use these data to address the petrogenesis of the high-Mg diorites and A-type rhyolites, and to elucidate the subduction history of the Proto-Tethys Ocean.

2. Reg a ge g

The Altun Orogenic Belt (AOB) is an important section of the Central China Orogenic Belt that lies between the Tarim to the north and the Kunlun Mountains and Qaidam to the south (Fig. 1a). The AOB consists of four E-W trending, subparallel tectonic units from north to south: (1) the northern Altun Archean complex zone (locally known as the North Altun terrane or Dunhuang block; Zhang et al., 2014), (2) the NAOB (previously called the northern Altun oceanic subduction-collision complex; Liu et al., 2012), (3) the central Altun block (CAB), and (4) the southern Altun continental subduction-collision complex zone that contains high- to ultrahigh-pressure and ophiolitic rocks (Liu et al., 2009) (Fig. 1b).

The NAOB extends ~300 km from east to west. It consists of high-pressure metamorphic rocks, ophiolites, mafic and felsic igneous rocks, and volcano-sedimentary sequences (Fig. 1c). The volcano-sedimentary sequence crops out along the NAOB, and is known as the Lapeiquan Formation (Group; Xinjiang BGMR, 2006). Previous investigations have suggested that the Lapeiquan Formation is an Ordovician (Xinjiang BGMR, 2006) or Mesoproterozoic sequence (Xinjiang

BGMR, 1981); however, recent zircon U-Pb ages from rhyolites (485-495 Ma) indicate a late Cambrian age (Wang et al., 2019; Ye et al., 2018). The ophiolites occur scarcely between the Lapeiquan and Hongliugou areas, and consist mainly of serpentinized peridotite, cumulates (wehrlite, anorthosite, gabbro, and plagiogranite), basalts, and silicalites (Yang et al., 2008). The cumulates yield zircon U-Pb ages of 520-480 Ma (Gai et al., 2015; Yang et al., 2008), and the ophiolites are thought to formed in a supra-subduction zone (Yang et al., 2008). The high-pressure metamorphic rocks are blueschists and eclogites that were metamorphosed at 510–490 Ma, and occur as tectonic blocks in the subduction–accretion complex (Zhang et al., 2010). The mafic intrusions yield ages of 520-460 Ma and are sparsely distributed along the NAOB (Ye et al., 2018). The granitic rocks in this area can be divided into two groups, i.e., ~520–470 Ma subduction-related group (mainly I-type granites) and ~450–410 Ma post-orogenic group (I- and S-type granites and adakitic rocks) (Han et al., 2012; Liu et al., 2016b, 2017a; Wu et al., 2009). The assemblage of high-pressure metamorphic rocks, ophiolites, subduction-accretion complex, and arc igneous rocks suggest that the NAOB was an early Paleozoic accretionary orogenic belt (Meng et al., 2017; Zhang et al., 2017).

3. Pe g a

3.1. Baijia ha di i e

The Baijianshan pluton was intruded into the lower member of the Lapeiquan Formation, and is in fault contact with Carboniferous sedimentary rocks (

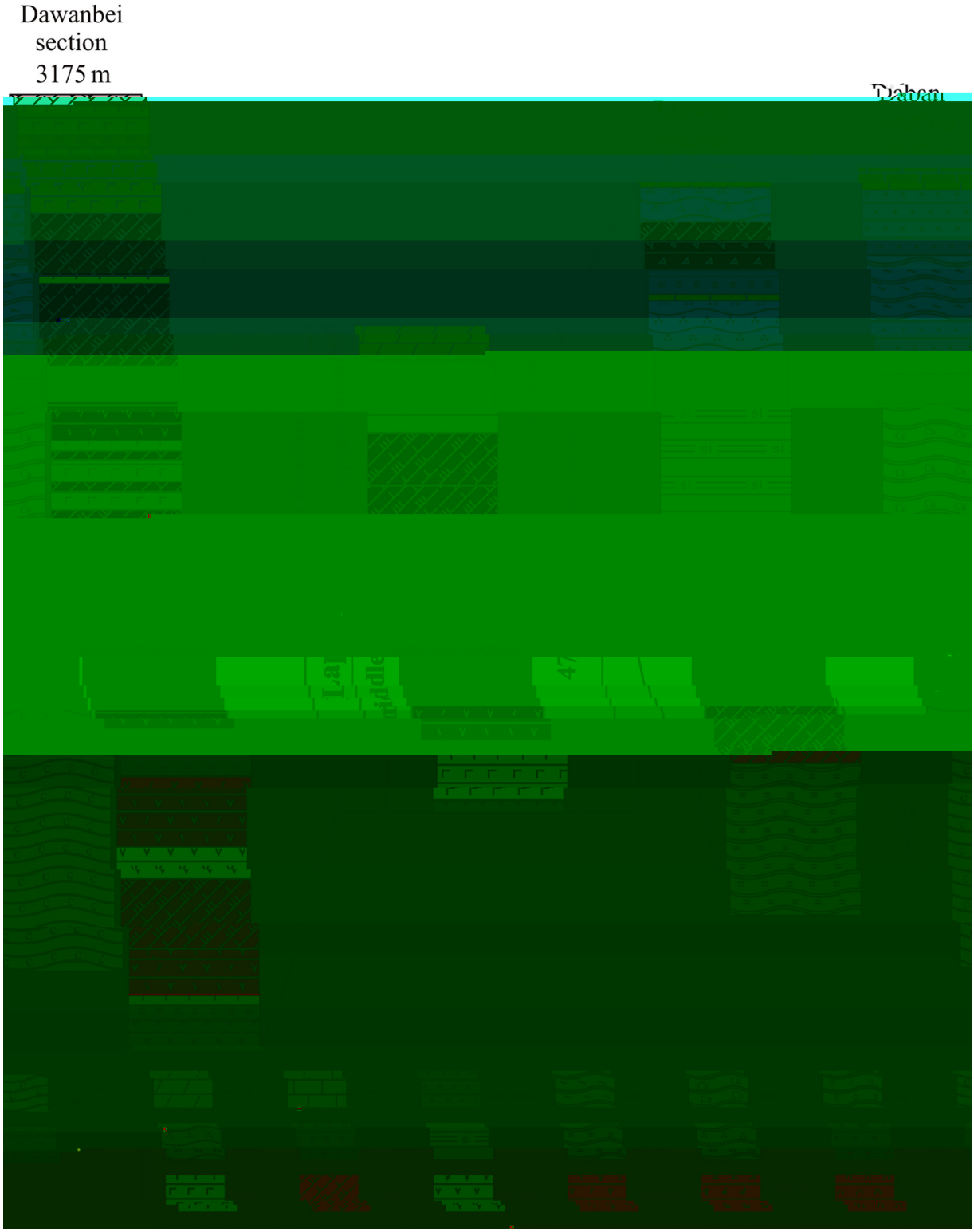

F g. 3. Measured section of the middle member and upper member of Lapeiquan Formation (data are from Xinjiang BGMR, 2006)

(UMLF) consists mainly of clastic rocks, cherts and carbonates, with minor meta-volcanic rocks (Fig. 2c, 3; Xinjiang BGMR, 2006; Ye et al., 2018). The volcano-sedimentary sequence of MMLF and UMLF extends for >100 km between the Qiongtag to Lapeiquan areas. Lower-greenschist-facies metamorphic minerals like sericite, chlorite, and biotite are commonly observed in most rocks.

Eight rhyolites for elemental analyses were chosen from the MMLF (Fig. 2a, b, 4c). Two rhyolite samples (16DBX01: 39°03′ 55″N, 91°42′36″E; 16DBX03: 39°04′12″N, 91°42′36″E) for zircon U–Pb dating and 11 rhyolite samples for geochemical analysis (Fig. 2a, c, 4d, e) were collected from the UMLF. All rhyolite samples were from fresh outcrops. We observed flow structures in the rhyolites from field observations and thin sections (e.g., Fig. 4c, e).

Fig. 4. Field photographs and photomicrographs of the Baijianshan diorties, Dawanbei and Dabanxi rhyolites. (a) The Baijianshan diorites intruded carbonate rocks; Field outcrop of the Baijianshan diorites (b) and Dawaibei rhyolites from the middle member of Lapeiquan Formation (c); (d, e) Interbedded layer rhyolites from the upper member of Lapeiquan Formation; (f, g) Euhedral plagioclase and amphibole in the thin section of the Baijianshan diorites (cross nicols); Phenocrysts and flow structure in the thin section of the Dawanbei rhyolites (h, i) and the Dabanxi rhyolites (j-l) (cross nicols). Abbreviations: Hb, hornblende; Kfs, K-feldspar; Pl, plagioclase; Q, quartz.

The rhyolites are pink-gray and porphyritic, and contain phenocrysts of quartz, perthite, and feldspar (20–25 vol.%) in a fine-grained groundmass (Fig. 4h–l). The matrix is composed of equigranular quartz (<0.05 mm; 50–60 vol.%), K-feldspar (15–20 vol.%), and biotite (2–5 vol.%) crystals (Fig. 4h–l).

4. A a ca e d

Zircon was separated first using magnetic and heavy liquid techniques, then hand-picking under a binocular microscope. Zircon grains were mounted in epoxy disks, which were polished to the approximate centers of the zircon grains. Cathodoluminescence (CL) images and transmitted light micrographs were obtained to investigate the internal structures. The three zircon samples were analyzed using laser ablation-inductively coupled plasma-mass spectrometry (LA-ICP-MS) method at Tianjin Institute of Geology and Mineral Resources, China Geological Survey (TIGMR, CGS). The laser beam diameter was set to be ~32 μm with a frequency of 10 Hz. Zircon 91500 and GJ-1 and glass NIST 610 were used as external standards. The analytical procedures

Tab e 1
Geochemical compositions of the Baijianshan diorites and Dawanbei and Dabanxi rhyolites.

Site	Baijianshan				Dawanbei			
Rock	Diorite	Diorite	Diorite	Diorite	Rhyolite	Rhyolite	Rhyolite	Rhyolite
Sample	16BJS04H1	16BJS04H2	16BJS04H3	16BJS04H4	16DWBH1	16DWBH2	16DWBH3	16DWBH4
SiO_2	57.65	56.47	56.34	56.39	75.83	72.25	74.17	78.55
TiO_2	0.71	0.61	0.98	0.61	0.16	0.17	0.16	0.15
Al_2O_3	16.33	16.04	16.44	16.15	11.75	14.17	12.26	10.25
$Fe_2O_3^T$	5.94	5.93	7.11	5.90	2.10	2.47	2.54	1.94
MnO	0.09	0.09	0.09	0.09	0.04	0.05	0.05	0.03
MgO	5.07	5.61	4.72	5.65	0.36	0.46	0.43	0.32
CaO	4.94	5.68	5.19	5.33	0.98	1.46	1.87	0.75
Na_2O	1.95	2.29	2.28	2.28	3.45	5.86	2.97	2.27
K_2O	3.91	3.42	3.04	3.36	4.05	1.91	4.22	4.72
P_2O_5	0.14	0.09	0.19	0.09	0.02	0.02	0.02	0.02
LOI	2.89	3.36	3.20	3.80	0.66	0.65	0.93	0.54
Total	99.6	99.6	99.6	99.7	99.4	99.5	99.6	99.5
$Mg^{\#}$	63	65	57	65	25	27	25	25
T_{zr}°C					811 ± 21	810 ± 22	800 ± 22	810 ± 19
Sc	14.8	17.1	14.4	16.9	4.57	5.30	4.88	3.97
V	103	109	156	115	1.64	2.94	2.54	1.53
Cr	15.3	40.1	47.1	41.9	2.03	5.00	4.40	6.23
Co	81.5	68.2	84.0	63.6	164	126	174	181
Ni	18.7	25.7	28.3	27.3	7.59	5.68	7.26	10.6
Ga	18.3	17.5	19.7	18.5	14.9	19.4	21.3	12.2
Rb	169	139	117	145	92.9	46.4	96.1	89.2
Sr	182	186	234	217	92.0	182	181	74.4
Y	23.3	34.4	27.7	29.9	47.1	53.9	61.0	42.0
Zr	185	177	263	175	304	332	306	279
Nb	15.8	15.5	15.9	15.2	19.6	21.0	19.8	18.9
Cs	4.96	6.27	3.53	4.93	0.190	0.104	0.196	0.181
Ba	543	585	577	485	1470	679	1720	1830
La	20.2	29.6	34.6	31.9	62.1	71.4	62.5	57.3
Ce	45.0	69.2	70.6	67.8	107	113	111	103
Pr	5.11	8.05	7.76	7.30	12.5	13.5	12.5	11.2
Nd	21.0	33.3	29.8	29.6	45.3	49.3	46.7	42.1
Sm	4.09	6.50	5.96	5.87	8.29	9.28	9.31	8.08
Eu	0.988	1.18	1.31	1.17	0.965	1.22	1.74	0.791
Gd	4.25	6.54	5.87	5.99	8.18	8.66	9.23	8.26
Tb	0.685	1.07	0.880	0.926	1.28	1.44	1.48	1.16
Dy	4.17	6.29	5.20	5.40	7.70	8.82	9.29	7.26
Ho	0.845	1.28	1.06	1.13	1.53	1.79	1.85	1.40
Er	2.49	3.65	3.04	3.36	4.88	5.64	5.88	4.38
Tm	0.356	0.531	0.426	0.477	0.705	0.811	0.780	0.661
Yb	2.41	3.44	2.85	3.10	4.88	5.76	5.90	4.64
Lu	0.358	0.526	0.421	0.462	0.728	0.845	0.842	0.661
Hf	4.63	4.70	6.08	4.68	7.88	8.62	8.16	7.48
Ta	1.28	1.36	1.23	1.30	1.72	1.70	1.70	1.62
Th	5.88	11.5	9.49	11.6	23.5	24.8	23.3	21.4
U	1.96	1.43	1.54	1.81	5.87	7.25	8.19	4.82

Site	Dawanbei				Dabanxi			
Rock	Rhyolite	Rhyolite	Rhyolite	Rhyolite	Rhyolite	Rhyolite	Rhyolite	Rhyolite
Sample	16DWBH5	16DWBH6	16DWBH7	16DWBH8	16DBX01H1	16DBX01H2	16DBX01H3	16DBX01H4
SiO_2	74.70	71.16	70.07	74.44	77.17	78.65	77.33	77.46
TiO_2	0.17	0.18	0.17	0.19	0.17	0.14	0.15	0.14
Al_2O_3	12.38	13.86	14.38	12.59	12.25	11.40	12.03	11.90
$Fe_2O_3^T$	2.72	3.25	3.07	2.58	1.44	1.22	1.74	1.64
MnO	0.05	0.07	0.06	0.05	0.03	0.03	0.04	0.03
MgO	0.58	0.51	0.53	0.48	0.55	0.45	0.63	0.62
CaO	1.10	2.60	2.54	1.70	0.26	0.21	0.25	0.23
Na_2O	4.25	5.29	5.97	5.06	5.89	5.23	5.76	5.42
K_2O	2.79	1.85	1.57	1.69	1.08	1.56	0.95	1.32
P_2O_5	0.02	0.02	0.02	0.02	0.02	0.02	0.02	0.02
LOI	0.74	0.89	1.18	0.85	0.70	0.55	0.83	0.79
Total	99.5	99.7	99.6	99.7	99.6	99.5	99.7	99.6
$Mg^{\#}$	30	24	25	27	43	42	42	43
T_{zr}°C	829 ± 21	785 ±24	779 ±24	814 ± 22	813 ± 18	809 ± 18	791 ± 17	807 ± 18
Sc	4.97	4.91	5.32	5.15	2.24	2.77	2.20	2.47
V	2.66	2.99	2.72	2.36	0.543	0.362	0.282	0.793
Cr	6.73	4.83	6.16	5.25	-1.23	-0.755	-1.56	-1.15
Co	152	124	99.5	134	230	236	192	219
Ni	11.3	6.51	5.35	5.29	10.2	8.60	6.87	8.18
Ga	17.2	25.3	22.3	18.7	18.9	19.3	17.9	20.5
Rb	67.5	47.1	44.5	44.1	25.6	30.3	16.3	36.6
Sr	124	286	249	172	61.5	70.9	60.6	57.8
Y	58.4	62.9	60.7	57.8	57.0	75.1	64.4	54.2

Tab e 1 (*c i ed*)

Site	Dawanbei				Dabanxi			
Rock	Rhyolite	Rhyolite	Rhyolite	Rhyolite	Rhyolite	Rhyolite	Rhyolite	Rhyolite
Zr	343	325	321	349	266	254	214	244
Nb	22.9	22.2	21.5	23.3	25.0	22.7	17.8	22.6
Cs	0.147	0.127	0.146	0.117	0.286	0.159	0.220	0.247
Ba	1100	683	484	554	523	785	561	701
La	72.2	66.0	62.3	70.5	56.9	47.0	53.4	61.5
Ce	122	120	111	124	87.0	91.9	93.5	93.2
Pr	14.3	13.4	12.3	14.0	11.6	11.3	11.3	12.4
Nd	52.5	50.2	45.2	51.4	48.3	44.3	44.6	47.1
Sm	9.56	9.56	8.52	9.99	9.41	10.4	9.19	8.17
Eu	1.14	1.44	1.32	1.14	0.942	1.04	1.05	0.857
Gd	9.29	9.52	8.75	9.37	10.0	10.9	10.6	8.51
Tb	1.52	1.56	1.42	1.54	1.68	1.93	1.78	1.43
Dy	9.37	9.94	9.39	9.18	10.1	12.1	11.0	8.64
Ho	1.98	2.11	1.94	1.96	2.26	2.63	2.21	2.00
Er	6.00	6.53	6.04	6.00	6.58	7.94	6.85	6.00
Tm	0.899	0.910	0.842	0.901	0.944	1.19	0.944	0.883
Yb	6.27	6.39	6.09	6.32	6.28	7.50	6.11	5.96
Lu	0.932	0.875	0.907	0.903	0.913	1.12	0.883	0.845
Hf	8.70	8.48	8.75	9.03	7.93	7.54	6.10	7.11
Ta	1.82	1.71	1.60	1.79	2.36	2.14	1.66	2.05
Th	26.0	24.8	23.9	26.7	20.2	21.7	16.7	17.9
U	7.01	7.83	7.60	6.92	5.15	5.61	5.47	4.65

Site	Dabanxi						
Rock	Rhyolite	Rhyolite	Rhyolite	Rhyolite	Rhyolite	Rhyolite	Rhyolite
Sample	16DBX01H5	16DBX01H6	16DBX03H1	16DBX03H2	16DBX03H3	16DBX03H4	16DBX03H5
SiO_2	76.44	61.19	74.99	77.23	74.49	74.75	78.58
TiO_2	0.16	1.34	0.16	0.13	0.16	0.16	0.14
Al_2O_3	12.23	14.40	12.56	11.68	13.23	12.97	10.57
$Fe_2O_3^T$	1.93	8.41	2.69	2.48	2.65	2.56	2.58
MnO	0.04	0.10	0.05	0.05	0.06	0.06	0.06
MgO	0.80	2.57	0.93	0.84	0.72	0.85	0.93
CaO	0.26	3.17	0.51	0.28	0.26	0.34	0.26
Na_2O	4.98	5.47	5.82	5.60	5.92	5.40	4.19
K_2O	1.73	0.90	1.18	0.98	1.74	2.14	1.63
P_2O_5	0.02	0.20	0.02	0.02	0.02	0.02	0.02
LOI	0.97	1.98	0.64	0.43	0.43	0.53	0.68
Total	99.6	99.7	99.6	99.7	99.7	99.8	99.6
$Mg^{\#}$	45	41	40	35	40	42	35
T_{zr}°C	807 ± 17	794 ± 19	788 ± 18	803 ± 19	801 ± 18	799 ± 16	798 ± 18
Sc	1.72	16.6	2.72	2.57	2.88	3.15	2.20
V	0.833	162	3.32	2.00	1.93	3.11	3.39
Cr	5.33	9.43	9.69	11.2	16.7	13.8	11.2
Co	186	89.5	1.64	1.47	1.39	1.46	1.48
Ni	7.78	7.87	2.40	3.31	3.29	4.66	2.59
Ga	20.6	20.0	19.9	18.9	20.8	20.5	19.5
Rb	35.4	23.6	26.2	20.8	41.0	49.8	37.0
Sr	53.1	195	57.8	56.2	67.3	60.2	58.6
Y	56.6	49.6	55.6	57.7	74.0	73.4	62.6
Zr	232	203	240	213	254	247	209
Nb	17.8	14.3	21.6	18.7	23.6	23.2	17.3
Cs	0.237	0.356	0.136	0.112	0.161	0.0993	0.165
Ba	845	301	1010	505	740	942	723
La	41.9	32.7	52.5	49.9	55.3	53.1	64.1
Ce	67.8	65.5	101	99.7	112	101	125
Pr	8.98	7.92	11.9	11.4	13.5	11.9	14.3
Nd	35.8	30.9	44.7	41.8	50.0	47.1	53.2
Sm	6.97	7.06	8.72	8.41	10.6	10.9	9.65
Eu	0.728	1.34	0.892	0.921	1.13	1.22	0.901
Gd	7.91	7.75	8.42	8.63	11.6	11.0	9.15
Tb	1.31	1.27	1.30	1.46	1.95	1.86	1.35
Dy	8.32	7.84	8.44	9.28	12.2	11.5	8.68

Tab e 2
Nd isotopic compositions of the Baijianshan diorites and Dawanbei and Dabanxi rhyolites.

Sample	Rock type	Sm(ppm)	Nd(ppm)	$^{147}Sm/^{144}Nd$	$^{143}Nd/^{144}Nd$ (2σ)	$(^{143}Nd/^{144}Nd)_i$	$\varepsilon_{Nd}(T)$	T_{DM}	T^C_{DM}
Baijianshan									
16BJS04H1	Diorite	4.09	21.0	0.1177	0.511924 (3)	0.511511	-8.5	1944	1948
16BJS04H2	Diorite	6.50	33.3	0.1180	0.511907 (3)	0.511493	-8.9	1976	1977
16BJS04H4	Diorite	5.87	29.6	0.1199	0.511900 (2)	0.511479	-9.1	2026	1998
Dawanbei									
16DWBH1	Rhyolite	8.29	45.3	0.1106	0.512348 (6)	0.511989	-0.2	1185	1262
16DWBH6	Rhyolite	9.56	50.2	0.1151	0.512339 (2)	0.511966	-0.7	1253	1285
16DWBH7	Rhyolite	8.52	45.2	0.1140	0.512343 (7)	0.511974	-0.5	1232	1276
Dabanxi									
16DBX01H1	Rhyolite	9.41	48.3	0.1178	0.512371 (2)	0.511989	-0.2	1237	1239
16DBX01H3	Rhyolite	9.19	44.6	0.1246	0.512396 (3)	0.511992	-0.2	1288	1213
16DBX03H2	Rhyolite	8.41	41.8	0.1216	0.512370 (4)	0.511976	-0.5	1290	1249
16DBX03H3	Rhyolite	10.6	50.0	0.1282	0.512403 (2)	0.511987	-0.2	1329	1209

Chondrite uniform reservoir (CHUR) values ($^{147}Sm/^{144}Nd$ = 0.1967, $^{143}Nd/^{144}Nd$ = 0.512638) are used for the calculation. λ_{Sm} = 6.54 × 10^{-12} $year^{-1}$ (Lugmair and Harti, 1978). The $(^{143}Nd/^{144}Nd)_i$, ε_{Nd}( ) of the 16BJS04, 16DWB and 16DBX were calculated using age of 536 Ma, 495 Ma and 495 Ma, respectively. The two-stage model age (T^C_{DM}) calculations are given by Jahn et al., 1999.

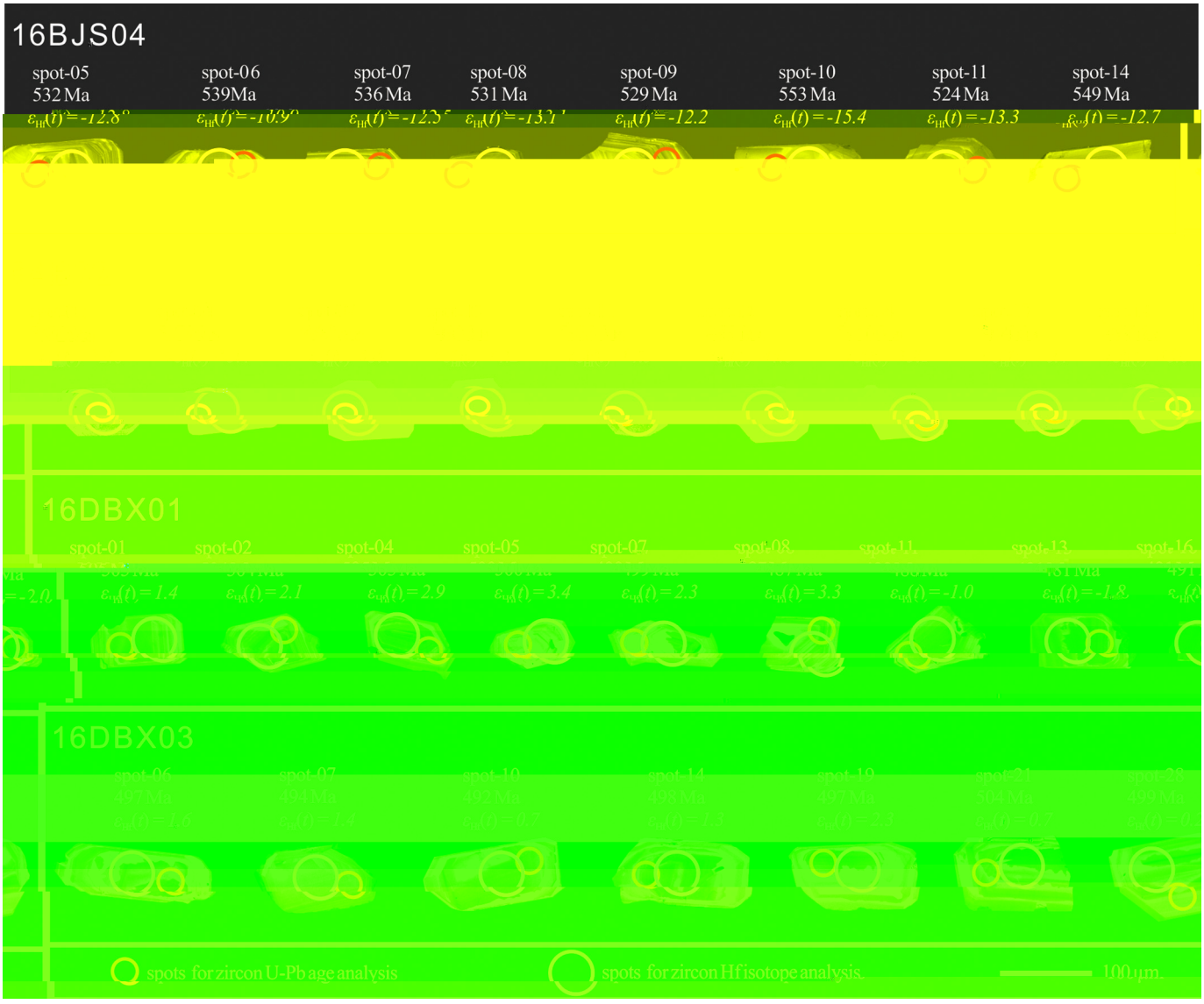

F g. 5. Representative CL images of zircon from the Baijianshan diorites (16BJS04), Dawanbei rhyolites (16AB02) from the middle Lapeiquan Formation, and the Dabanxi rhyolites (16DBX02 and 16DBX03) from the upper Lapeiquan Formation. Analytical spots, ages and ε_{Hf}( ) are shown (see details in the text).

were given by Geng et al. (2011). ICPMSDataCal and Isoplot/Ex 3.23 were used for data reduction (Liu et al., 2010) and processing (Ludwig, 2003), respectively. The age data are presented in Ap-

size of 60 μm. Instrumental parameters and data acquisition were similar to those documented in Geng et al. (2011). Zircon Hf isotopic compositions are listed in Appendix Table II.

Whole-rock major and trace element compositions were determined by a Rigaku ZSX100e XRF and PerkinElmer ELAN DRC-e ICP–MS at the State Key Laboratory of Ore Deposit Geochemistry, Institute of Geochemistry, Chinese Academy of Sciences (CAS), following Li et al. (2002) and Qi et al. (2000), respectively. The analytical precision was better than 5% for major elements and 10% for most trace elements, and the results are reported in Table 1.

Samples for Nd isotopic analysis were dissolved in mixture of HF, HNO_3 and $HClO_4$ in Teflon bombs, then separated using conventional cation-exchange techniques. The isotopic measurements were performed on a Thermo Scientific Triton thermal ionization mass spectrometer (TIMS) at the TIGMR, CGS. Mass fractionation corrections for Nd isotope ratios assumed a $^{146}Nd/^{144}Nd$ ratio of 0.7219. The mean $^{143}Nd/^{144}$

high-Mg andesites in the Setouchi Volcanic Belt (SVB), Japan (Fig. 8d; Tatsumi et al., 2006).

The Baijianshan diorites have total rare earth element (REE) contents of 112-171 ppm, with enrichment in light REE (LREE) relative to heavy REE (HREE; La_N/Yb_N = 5.7-8.2) and moderately negative Eu anomalies (Eu/Eu^* = 0.55-0.72; Fig. 9a). The

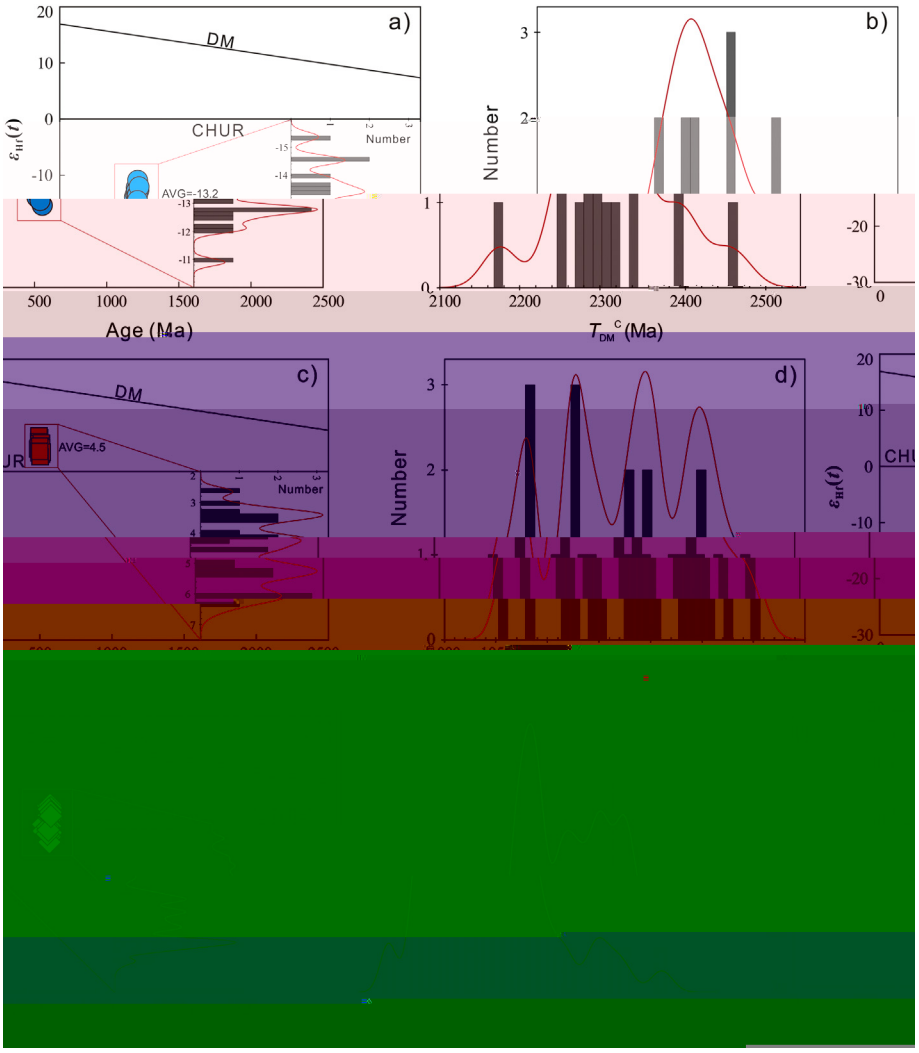

Fig. 11. Zircon age versus zircon ε_{Hf}( ) (histograms of zircon ε_{Hf}( ) insert) and histograms of T_{DM}^{C} for the Baijianshan diorites (a, b), Dawanbei rhyolites (c, d) and Dabanxi rhyolites (e, f).

model ages (T_{DM}^{C}) are 2463-2176 Ma, with a weighted mean age of 2314 Ma (Fig. 11b).

The $^{176}Hf/^{177}Hf$ ratios of zircons from the Dawanbei rhyolites range from 0.282555 to 0282666, and their $^{176}Lu/^{177}Hf$ ratios are low (~0.002). The zircon ε_{Hf}( ) values are 2.6 to 6.4 (Fig. 10b), with a weight mean of 4.5 (Fig. 11c). The Hf model ages range from 1059 Ma to 1299 Ma (Fig. 11d).

The zircon grains from the Dabanxi rhyolites have $^{176}Hf/^{177}Hf$ ratios of 0.282433-0.282581, which correspond to initial $^{176}Hf/^{177}Hf$ ratios of 0.282397-0.282563 and ε_{Hf}( ) values of -2.3 to +3.4 (weight mean = +1; Fig. 9e, 10b). The Hf model ages are 1606-1245 Ma (Fig. 11f). On an ε_{Nd}( ) versus ε_{Hf}( ) diagram, the diorites and rhyolites show broadly coupled whole-rock Nd and zircon Hf isotopic compositions (Fig. 10c).

6. D c

6.1. Pe ge e i f he Baijia ha di i e

The Baijianshan high-Mg diorites have crustal-like trace element patterns (Fig. 9b, d) and enriched whole-rock Nd and zircon Hf isotopic compositions (Fig. 10a, b), indicating contribution of continental component to their petrogenesis, related to either source variation or crustal contamination during magma fractionation (e.g. Jahn et al., 1999). However, the following lines of evidence argue against the view of crustal assimilation: (1) the constant whole-rock Nd and zircon Hf isotopic compositions (Table 2), (2) the large range of Nb/La ratios but constant Nb/Th ratios in most samples (Table 1), and (3) the absence of xenocrystic zircons (e.g. Yang et al., 2019; Fig. 5; Appendix Table I). The limited extent of crustal contamination means that the geochemical characteristics of the Baijianshan diorites directly reflect their source and tectonic environment.

High-Mg andesites and diorites could be generated by a variety of processes, including partial melting of hydrous peridotite (Hirose, 1997; Straub et al., 2011; Wang et al., 2014), partial melting of lower continental crust and interaction with overlying mantle through delamination (Gao et al., 2004; Wang et al., 2006), mixing between mantle-derived mafic and crust-derived felsic magmas at crustal-level (Qian and Hermann, 2010; Shellnutt and Zellmer, 2010), and interactions between subducted sediments or slab melts and peridotite in the mantle wedge (Tatsumi, 2001; Wang et al., 2011).

Experimental studies have demonstrated that partial melting of the hydrous mantle peridotite at temperatures below 1100 °C at 1 GPa can produce high-Mg andesitic melt with low FeO^{T} (4.04–5.36 wt.%) and

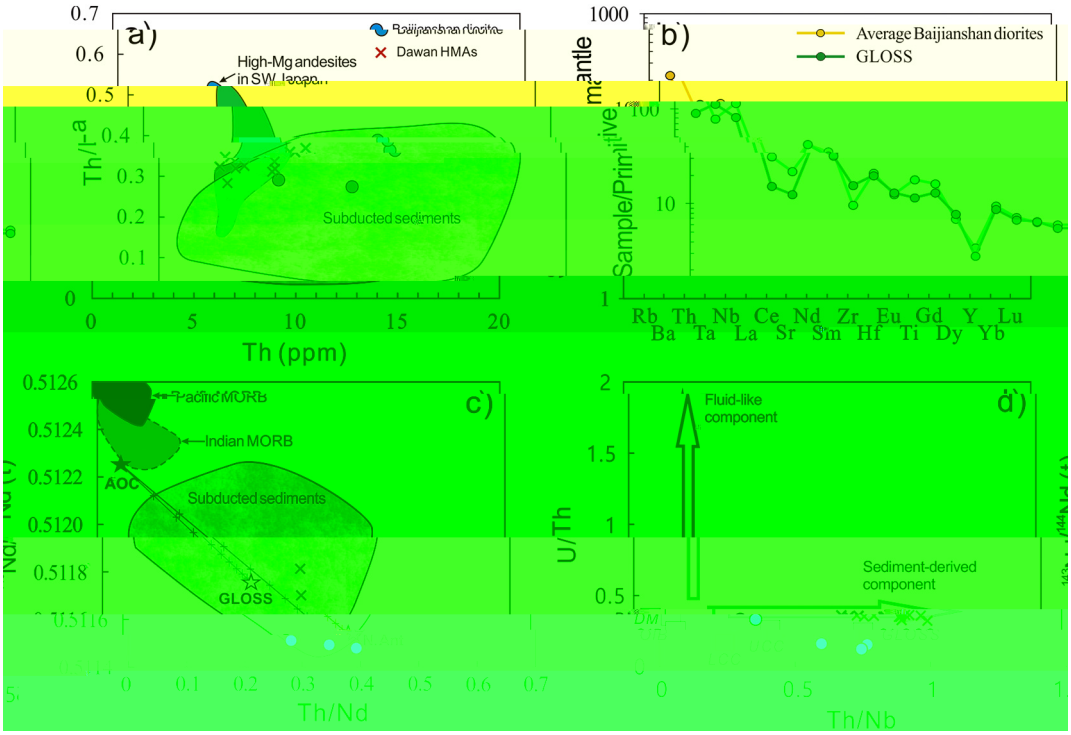

F g. 12. (a) Th versus Th/La diagram for the Baijianshan diorites; (b) Primitive mantle-normalized trace-element spider diagrams for the Baijianshan diorites and GLOSS; (c) Plot of Th/Nd versus $^{143}Nd/^{144}Nd(t)$; (d) Th/Nb versus U/Th diagrams for the Baijianshan diorites. Data for GLOSS and subducted sediments are from Plank and Langmuir (1998), other data sources are same as Fig. 6.

TiO_2 (0.55–0.70 wt.%), and high CaO (8.53–9.99 wt.%) and Al_2O_3 (17.2–21.7 wt.%) contents (Hirose, 1997; Rapp et al., 1999). In this scenario, high-Mg diorites commonly contain dunite xenoliths and high-Fo olivine xenocrysts (e.g. Qian and Hermann, 2010). The absence of olivine xenocrystal and dunite xenoliths, combined with high Al_2O_3 (16.04-16.44 wt.%), low CaO (4.94-5.68 wt.%) and negative $\varepsilon_{Nd}(\ )$ values indicate that the Baijianshan diorites were not generated from partial melting of hydrated peridotite.

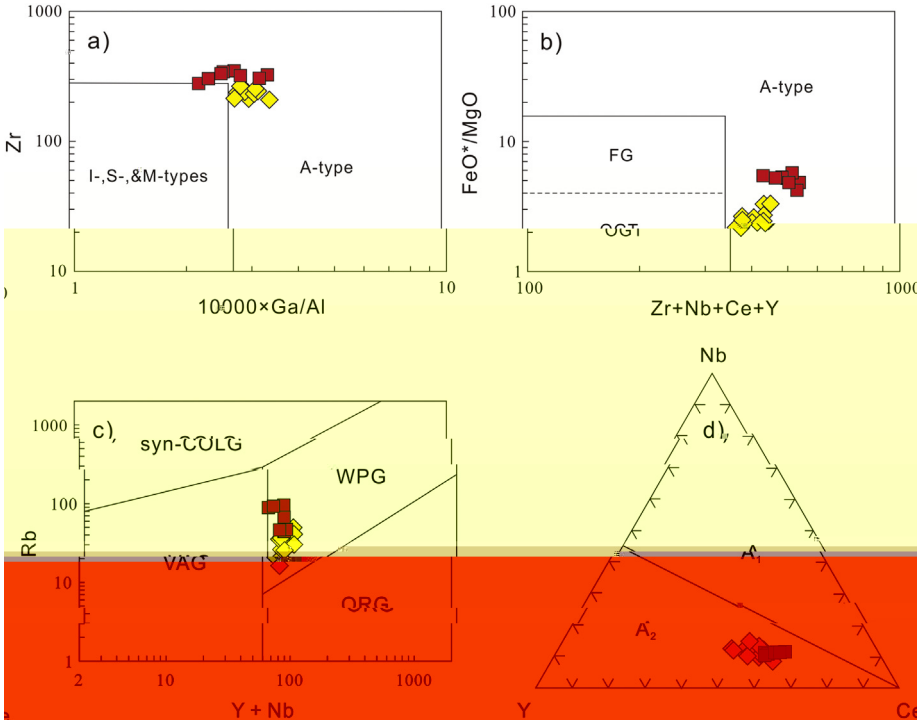

F g. 13. (a) 10000 × Ga/Al versus Zr and (b) (Zr + Nb + Ce + Y) versus FeO^*/MgO discrimination diagrams of Whalen et al. (1987), indicative of the Dawanbei and Dabanxi rhyolites are A-type granites. (c) Y + Nb versus Rb diagram of Pearce, 1996 showing the Dawanbei and Dabanxi rhyolites plot into the WPG field. (d) Plots of Dawanbei and Dabanxi A-type rhyolites in Nb-Y-Ce triangular diagram of Eby (1992) within the field of A_2-type granites. FG-fractionated felsic granites, OGT-unfractionated, VAG-volcanic arc granites, ORG-ocean ridge granites, WPG-within-plate granites, syn-COLG-syn-collision granites, A_1-anorogenic A-type granites, A_2-post-collisional A-type granites.

The MgO contents and $Mg^{\#}$ of the diorites are higher than those of experimental melts of metabasalt and eclogite at 1.0-4.0 GPa (Fig. 8c, d; Qian and Hermann, 2013; Rapp and Watson, 1995; Rapp et al., 1999), suggesting that partial melting of delaminated or eclogitic thickened lower continental crust did not generate the Baijianshan diorites, despite their crust-like elemental and isotopic signatures. Partial melting of lower continental crust generally produces adakitic magmas with high Sr and low Y and Yb contents (Qian and Hermann, 2013; Wang et al., 2008). In contrast, the Baijianshan diorites have relatively low Sr (182-234 ppm) and high Y (23.3-34.4 ppm) and Yb (2.41-3.44 ppm) contents. Furthermore, lower continental crust has low U (0.2 ppm) and Th (1.2 ppm) contents (Rudnick and Gao, 2003), unlike the Baijianshan diorites (U = 1.43-1.96 ppm, Th = 5.88-11.6 ppm).

The relatively uniform whole-rock ε_{Nd}( ) and zircon ε_{Hf}( ) compositions (Fig. 10a, b) of the Baijianshan diorites are in contrast with those expected for hybrid magmas. Moreover, MORB-like basaltic melts assimilated by crustal melts would require large volumes of continental crust to achieve the enriched Nd–Hf compositions of the Baijianshan diorites, which is impossible given the high MgO contents and $Mg^{\#}$ of these rocks. The absence of any mafic microgranular enclaves (MMEs) in the Baijianshan diorite pluton also precludes the crustal level magma mixing model.

The following lines of evidence show that interaction between subduction-related components and the overlying mantle wedge can account for the formation of the Baijianshan diorites. (1) The Baijianshan diorites are high-K calc-alkaline and have high K_2O contents (Fig. 8a, b) resembling high-Mg andesites in the SVB, which were formed by the interaction between subducted sediment-derived melts and peridotites (Tatsumi, 2001; Wang et al., 2011; Yang et al., 2019). (2) The diorites have a crust-like geochemical signature (Fig. 9a, b), enriched whole-rock ε_{Nd}( ) and zircon ε_{Hf}( ) values (Fig. 10a, b), and their coupled Nd-Hf isotopic compositions that overlap with those of typical marine sediments (Fig. 10c). (3) The Baijianshan diorites have high Th contents and Th/La ratios, which plot in the subducted sediments field on a Th/La versus Th diagram (Fig. 12a). In addition, the Baijianshan diorite composition is similar to that of Global Subducting Sediment (GLOSS; Fig. 12b; Plank and Langmuir, 1998). The low ε_{Nd}( ) values and high Th/Nd ratios are also consistent with those of subducted sediments (Fig. 12c), suggesting a major contribution by subducted sediments. (4) The Baijianshan diorites have consistently low U/Th (0.12–0.33) and high Th/Nb (0.37–0.77) ratios, which also support the involvement of a sediment-derived melts rather than of slab-derived fluids (Fig. 12d). According to the evidence above, we argue that the Baijianshan diorites were generated by the melting of subducted sediments and that the melts interacted with peridotites in the mantle wedge.

Three competing mechanisms should be taken into account in explaining the genesis of the Baijianshan high-Mg diorite: (1) mid-ocean ridge subduction (e.g., Sun et al., 2009; Windley et al., 2007), (2) slab break-off (e.g., van Hunen and Allen, 2011) or (3) slab roll-back (Hawkins et al., 1990; Yan et al., 2016). Lack of coeval adakites, boninites, and HT/LP metamorphic rocks in the NAOB clearly contradicts the mid-ocean ridge subduction model (Kusky et al., 2003). Furthermore, no evidence supports the occurrence of early Cambrian collision in the NAOB. Instead, the subduction most likely lasted until ~460 Ma in this area (Han et al., 2012; Ye et al., 2018). Thus, the slab break-off model cannot satisfactorily describe the origin of the Baijianshan high-Mg diorites. The Dawan high-Mg andesites/diorites are regarded as the consequence of the slab roll-back, which formed at ~490 Ma (Meng et al., 2017; Ye et al., 2018). Thus, the much older (~535 Ma) Baijianshan diorites are unlikely applicable this model.

We propose that the Baijianshan high-Mg diorites were formed by partial melting of subducted sediments at the early stage, possibly the initial stage of oceanic subduction. Firstly, the ε_{Nd}( ) and ε_{Hf}( ) values of the granitoids derived gradually from enrichment to depletion from early to late (Fig. 8a, b), suggesting continuous increasing of mantle-derived material (or/and juvenile crust input) during subduction (e.g. Liu et al., 2017). Secondly, The age of ~535 Ma is earlier than previous reported subduction-related rocks (520-460 Ma) (Han et al., 2012; Liu et al., 2016b; Meng et al., 2017; Wu et al., 2009; Ye et al., 2018; Zheng et al., 2019) ophiolites (480-520 Ma) (Gai et al., 2015; Yang et al., 2008) and high-pressure and low-temperature (HP/LT) metamorphic rocks (490-510 Ma) (Zhang et al., 2010) in the NAOB. Therefore, we suggest that the subduction in the NAOB began at ~535 Ma.

6.2. Pe ge e i f he Da a bei a d Daba i h li e

Based on the nature of their protolith and the pressure and temperature of melting, silicic igneous rocks are generally subdivided into A-, I-S-, and M-types (Bonin, 2007). Several geochemical approaches have been made to discriminate between A-type granites and others (Eby, 1992; Whalen et al., 1987), including high $Na_2O + K_2O$ contents and Ga/Al and molar Fe/Mg ratios, low CaO content, enriched in HFSE, and depleted in Sr and Eu (Bonin, 2007; Whalen et al., 1987). On a 10000 × Ga/Al versus Zr diagram, the Dawanbei and Dabanxi rhyolites plot in the field of A-type granites (Fig. 13a; Whalen et al., 1987). Although highly fractionated granites can yield high FeO^T/MgO ratios, the Dawanbei and Dabanxi rhyolites plot within the A-type field on the (Zr + Nb + Ce + Y) versus FeO^T/MgO diagram, which is generally used to distinguish A-type from highly differentiated granites (Fig. 13b). On the Yb + Nb versus Rb diagram of Pearce, 1996, these rhyolites plot in the WPG field (Fig. 13c) are classified as A_2 subtype according to the classification of Eby (1992) (Fig. 13d). The calculated zircon saturation temperatures of the Dawanbei and Dabanxi rhyolites are 779 °C to 829 °C (Table 1; weighted mean = 803 °C). Therefore, the A-type signature of the Dawanbei and Dabanxi rhyolites was further supported by relatively high temperature.

The Dawanbei and Dabanxi rhyolites most have low K_2O (0.95-2.79 wt.%) contents with K_2O/Na_2O ratios of 0.16-0.66 (Table 1). Such low-K silicic rocks (e.g. trondhjemite and tonalite) could be formed either through fractional crystallization of basaltic magmas or through partial melting of basaltic rocks in the crust (e.g. Atherton and Petford, 1993; Rapp and Watson, 1995; Thy et al., 1990). We rule out fractional crystallization of mafic magma base on the following evidence: (1) the whole-rock ε_{Nd}( ) values and trace-element ratios (e.g. U/Zr, Nb/Zr, and Th/Zr) of the Dawanbei and Dabanxi rhyolites are remarkably different from those of contemporaneous basalts and mafic intrusions (Fig. 10a), (2) there exists a clear compositional gap between the basalts and the rhyolites (Fig. 8), and (3) the volume of the rhyolites is far greater than that of the basalts (Fig. 3).

We favor an alternative explanation for the formation of the Dawanbei and Dabanxi rhyolites: the partial melting of mafic rocks. Many melting experiments conducted on mafic rocks at pressures of 1-38 kbar indicate pressure plays a key role in controlling melt composition (Beard, 1995; Beard and Lofgren, 1991; Qian and Hermann, 2013; Rapp et al., 1999; Rapp and Watson, 1995; Thy et al., 1990). Partial melting of basaltic rocks generally produces adakitic magmas at 10-38 kbar (Qian and Hermann, 2013; Rapp et al., 1999; Rapp and Watson, 1995; Sen and Dunn, 1994) and high-K silicic melts resembling calc-alkaline I-type granites at 7-8 kbar (Rapp and Watson, 1995; Sisson et al., 2005). Dehydration melting of basaltic rocks at shallow crustal levels (1-3 kbar) yields metaluminous to mildly peraluminous granodioritic to trondhjemitic melts (Beard and Lofgren, 1991; Thy et al., 1990). We attribute the high SiO_2 and Na_2O, and low K_2O contents of the Dawanbei and Dabanxi rhyolites to low-degree partial melting of a basaltic source, suggesting the melting temperature was ~900 °C, based on experimental results (Beard and Lofgren, 1991). Thus, the Dawanbei and Dabanxi rhyolites were likely generated by shallow (1-3 kbar) dehydration melting of basaltic rocks at ~900 °C. Reaching this melting temperature at such shallow depths requires external heat input; therefore, these A-type rhyolites were likely generated in an extensional environment,

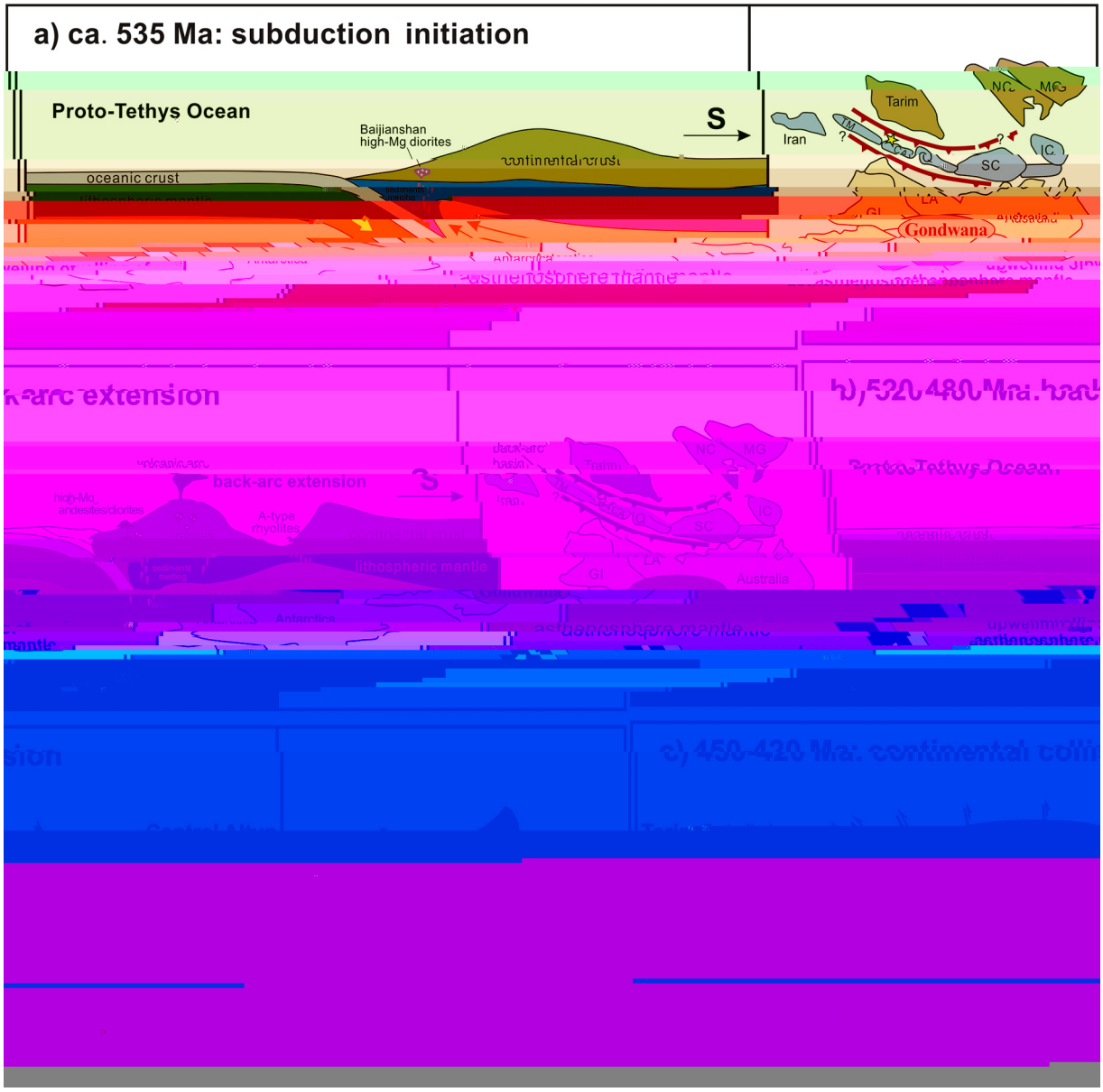

F g. 14. A schematic diagram to illustrate the tectonic evolution of the NAOB (see details in text). Abbreviations: TM-Tianshuihai-Mazar terrane, CA-Central Altun, GI-great India, LA-Lhasa terrane, Q-Qaidam, SC-South China, NC-North China, MG-Mongolia, IC-Indochina.

where the crust tends to be thin and magmatic advection of heat can reach shallow crustal levels.

The Dawanbei and Dabanxi rhyolites have pronounced negative Sr, Eu, and Ti anomalies (Fig. 9c-f). According to experimental studies, the residuum left after dehydration melting of mafic rocks is plagioclase-rich (~50%), with apatite, ilmenite, and magnetite (Beard and Lofgren, 1991; Thy et al., 1990); therefore, we suggest that the significant negative Sr, Eu, and Ti anomalies in the Dawanbei and Dabanxi rhyolites are related to residual plagioclase and Ti-Fe oxides, respectively.

It is generally accepted that A-type granitoids are genetically related to non-compressional regimes such as rifting or extensional environment (Eby, 1992; Whalen et al., 1987). Based on the geochemical subdivision of A-type granites by Eby (1992), the Dawanbei and Dabanxi rhyolites belong to A_2-subtype rocks (Fig. 13d). Their Y/Nb (2.22-3.63) and Yb/Ta (2.66-4.99) ratios are similar to those of IAB (Table 1). Furthermore, basalts from the bimodal volcanic sequence have high Zr (77.6-267 ppm), Nb (5.12-12.2 ppm), and Y (26.8-63.5 ppm) contents and Ti/Y (213-301), Gd/Yb (1.63-2.26) ratios, and low Hf/Ta (6.0-9.1) ratios (Hao et al., 2013), distinguishes those rocks from MORB, OIB and IAT, but resembles back-arc basin basalts (BABB) in the Okinawa Trough. The occurrence of a back-arc basin is compatible with the sedimentary features of the upper member of Lapeiquan Formation (Fig. 3). Thus, the bimodal volcanic rocks emplaced during syn-rifting stage and the marine clastic sequence deposited during post-rifting stage, resembles the evolution history of the Okinawa Trough (Sibuet et al., 1987). Thus, the Dawanbei and Dabanxi A-type rhyolites were likely formed in a continental back-arc setting.

6.3. Tec ic i lica i

The assembly of Gondwana was completed with the closure of the Mozambique Ocean (650–530 Ma) and the associated amalgamation of East and West Gondwana during the Pan-African Orogeny (Li et al., 2018a), which led to the final docking of Antarctica, Australia, and Southern Africa with previously amalgamated India and East Africa along the Kuunga (Pinjarra) Orogen (Collins and Pisarevsky, 2005;

Meert, 2003). From late Neoproterozoic to early Cambrian, Gondwana was split into several continental blocks primarily by the Proto-Tethys and Iapetus oceans; the former separated Gondwana from the North China, South China, Tarim blocks, and several microcontinental blocks (e.g. Qaidam, Alax, Dunhuang, and etc) and the latter separated Gondwana from Laurentia and Baltica. Recent studies of East Asia have indicated that the Tarim, Dunhuang, Alax and North China blocks were located north of the Proto-Tethys Ocean, while numerous scattered continental and micro-continental blocks were found south of the Proto-Tethys Ocean (including the South China, Indochina, Tianshuihai–

Bonin, B., 2007. A-type granites and related rocks: Evolution of a concept, problems and prospects. Lithos 97, 1–29.
Boynton, W.V., 1984. Geochemistry of the rare earth elements: Meteorite studies. In: Henderson, P. (Ed.), Rare Earth Element Geochemistry. Elservier, pp. 63–114.
Chen, Y.X., Song, S.G., Niu, Y.L., Wei, C.J., 2014. Melting of continental crust during subduction initiation: a case study from the Chaidanuo peraluminous granite in the North Qilian suture zone. Geochim. Cosmochim. Acta 132, 311–336.
Collins, A.S., Pisarevsky, S.A., 2005. Amalgamating eastern Gondwana: the evolution of the Circum-Indian Orogens. Earth Sci. Rev. 71, 229–270.
Crameri, F., Magni, V., Domeier, M., Shephard, G.E., Chotalia, K., Cooper, G., Eakin, C.M., Grima, A.G., Gürer, D., Király, Á., Mulyukova, E., 2020. A transdisciplinary and community-driven database to unravel subduction zone initiation. Nat. Commun. 11, 1–14.
Defant, M.J., Drummond, M.S., 1990. Derivation of some modern arc magmas by melting of young subducted lithosphere. Nature 347, 662–665.
Dong, Y.P., Zhang, G.W., Hauzenberger, C., Neubauer, F., Yang, Z., Liu, X., 2011. Palaeozoic tectonics and evolutionary history of the Qinling orogen: evidence from geochemistry and geochronology of ophiolite and related volcanic rocks. Lithos 122, 39–56.
Eby, G.N., 1992. Chemical subdivision of the A-type granitoids-petrogenetic and tectonic implications. Geology 20, 641–644.
Ewart, A., Collerson, K., Regelous, M., Wendt, J., Niu, Y., 1998. Geochemical evolution within the Tonga-Kermadec-Lau arc-back-arc systems: the role of varying mantle wedge composition in space and time. J. Petrol. 39, 331–368.
Gai, Y.S., Liu, L., Kang, L., Yang, W.Q., Liao, X.Y., Wang, Y.W., 2015. The origin and geologic significance of plagiogranite in ophiolite belt at North Altyn Tagh. Acta Petrol. Sin. 31, 2549–2565 (in Chinese with English abstract).
Gao, S., Rudnick, R.L., Yuan, H.L., Liu, X.M., Liu, Y.S., Xu, W.L., Ling, W.L., Ayers, J., Wang, X.C., Wang, Q.H., 2004. Recycling lower continental crust in the North China Craton. Nature 432, 892–897.
Geng, J.Z., Li, H.K., Zhang, J., Zhang, Y.Q., 2011. Zircon Hf isotope analysis by means of LA-MC-ICP-MS. Geol. Bull. Chin. 30, 1508–1513 (in Chinese with English abstract).
Gueydan, F., Brun, J.P., Phillippon, M., Noury, M., 2017. Sequential extension as a record of Corsica Rotation during Apennines slab roll-back. Tectonophysics 710, 149–161.
Hall, C.E., Gurnis, M., Sdrolias, M., Lavier, L.L., Müller, R.D., 2003. Catastrophic initiation of subduction following forced convergence across fracture zones. Earth Planet. Sci. Lett. 212, 15–30.
Han, F.B., Chen, B.L., Cui, L.L., Wang, S.X., Chen, Z.L., Jiang, R.B., Li, L., Qi, W.X., 2012. Zircon SHRIMP U-Pb ages of intermediate-acid intrusive rocks in Kaladawan aera, eastern Altun Mountains, NW China, and its implications. Acta Petrol. Sin. 28, 2277–2291 (in Chinese with English abstract).
Hao, R.X., Chen, B.L., Chen, Z.L., Wang, Y., Li, S.B., Han, F.B., Zhou, Y.G., 2013. Geochemical characteristics of basalts from kaladawan in East Altun Mountains of Xinjiang and their implications. Acta Geosci. Sin. 34, 307–317 (in Chinese with English abstract).
Hawkins, J.M., Lonsdale, P.E., MacDougall, J.D., Volpe, A.M., 1990. Petrology of the axial ridge of the Mariana Trough back-arc spreading center. Earth Planet. Sci. Lett. 100, 226–250.
Hirose, K., 1997. Melting experiments on lherzolite KLB-1 under hydrous conditions and generation of high-magnesian andesitic melts. Geology 25, 42–44.
Jahn, B.M., Wu, F.Y., Lo, C.H., Tsai, C.H., 1999. Crust–mantle interaction induced by deep subduction of the continental crust: geochemical and Sr–Nd isotopic evidence from post-collisional mafic–ultramafic intrusions of the northern Dabie complex, central China. Chem. Geol. 157, 119–146.
Keenan, T.E., Encarnacion, J., Buchwaldt, R., Fernandez, D., Mattinson, J.M., Rasoazanamparany, C., Luetkemeyer, P.B., 2016. Rapid conversion of an oceanic spreading center to a subduction zone inferred from high-precision geochronology. Proc. Natl. Acad. Sci. U. S. A. 113 (47).
Kusky, T.M., Bradley, D., Donley, D.T., Rowley, D., Haeussler, P.J., 2003. Controls on intrusion of near-trench magmas of the Sanak-Baranof belt, Alaska, during Paleogene ridge subduction, and consequences for forearc evolution. Geological Society of America Special Papers 371, 269–292.
Li, X.H., Liu, Y., Tu, X.L., Hu, G.Q., Zen, W., 2002. Precise determination of chemical compositions in silicate rocks using ICP-AES and ICP-MS: a comparative study of sample digestion techniques of alkali fusion and acid dissolution. Geochimica 31, 289–294 (in Chinese with English abstract).
Li, Y., Yang, J.S., Dilek, Y., Zhang, J., Pei, X.Z., Chen, S.Y., Xu, X.Z., Li, J.Y., 2015. Crustal architecture of the Shangdan suture zone in the early Paleozoic Qinling orogenic belt, China: record of subduction initiation and backarc basin development. Gondwana Res. 27, 733–744.
Li, S.Z., Zhao, S.J., Liu, X., Cao, H.H., Yu, S.Y., Li, X.Y., Somerville, I., Yu, S.Y., Suo, Y.H., 2018a. Closure of the Proto-Tethys Ocean and Early Paleozoic amalgamation of microcontinental blocks in East Asia. Earth Sci. Rev. 186, 37–75.
Li, Y.C., Xiao, W.J., Tian, Z.H., 2018b. Early Palaeozoic accretionary tectonics of West Kunlun Orogen: insights from Datong granitoids, mafic-ultramafic complexes, and Silurian-Devonian sandstones, Xinjiang, NW China. Geol. J. 54, 1505–1517.
Liu, L., Wang, C., Chen, D., Zhang, A., Liou, J.G., 2009. Petrology and geochronology of HP–UHP rocks from the South Altyn Tagh, northwestern China. J. Asian Earth Sci. 35, 232–244.
Liu, Y.S., Hu, Z.C., Zong, K.Q., Gao, C.G., Gao, S., Xu, J., Chen, H.H., 2010. Reappraisement and refinement of zircon U-Pb isotope and trace element analyses by LA-ICP-MS. Chin. Sci. Bull. 55, 1535–1546.
Liu, J.H., Liu, L., Gai, Y.S., Kang, L., Yang, W.Q., Liao, X.Y., Yang, M., 2017. Zircon U-Pb dating and Hf isotopic compositions of the Baijianshan granodiorite in north Altyn Tagh and its geological significance. Acta Geologica Sinica 91, 1022–1038.
Liu, L., Wang, C., Cao, Y.T., Chen, D.L., Kang, L., Yang, W.Q., Zhu, X.H., 2012. Geochronology of multi-stage metamorphic events: Constraints on episodic zircon growth from the UHP eclogite in the South Altyn, NW China. Lithos 136, 10–26.
Liu, L., Liao, X.Y., Wang, Y.W., Wang, C., Santosh, M., Yang, M., Zhang, C.L., Chen, D.L., 2016a. Early Paleozoic tectonic evolution of the North Qinling Orogenic Belt in Central China: Insights on continental deep subduction and multiphase exhumation. Earth Sci. Rev. 159, 58–81.
Liu, C., Wu, C., Gao, Y., Lei, M., Qin, H., 2016b. Age, composition, and tectonic significance of Paleozoic granites in the Altyn orogenic belt, China. Int. Geol. Rev. 58, 131–154.
Liu, K., Zhang, J.J., Wilde, S.A., Zhou, J.B., Wang, M., Ge, X.H., Wang, J.M., Ling, Y.Y., 2017. Initial subduction of the Paleo-Pacific Oceanic plate in NE China: Constraints from whole-rock geochemistry and zircon U–Pb and Lu–Hf isotopes of the Khanka Lake granitoids. Lithos 274–275, 254–270.
Liu, X.Q., Zhang, C.L., Ye, X.T., Zou, H., Hao, X.S., 2019. Cambrian mafic and granitic intrusions in the Mazar-Tianshuihai terrane, West Kunlun Orogenic Belt: Constraints on the subduction orientation of the Proto-Tethys Ocean. Lithos 350–351, 105226.
Ludwig, K.R., 2003. User's Manual for Isoplot 3.00: a Geochronological Toolkit for Microsoft Excel. Kenneth R. Ludwig.
Lugmair, G.W., Harti, K., 1978. Lunar initial $^{143}Nd/^{144}Nd$: differential evolution of the lunar crust and mantle. Earth Planet. Sci. Lett. 39, 349–357.
Magni, V., Allen, M.B., van Hunen, J., Bouilhol, P., 2017. Continental underplating after slab break-off. Earth Planet. Sci. Lett. 474, 59–67.
Matte, P., Tapponnier, P., Arnaud, N., Bourjot, L., Avouac, J.P., Vidal, P., Liu, Q., Pan, Y.S., Wang, Y., 1996. Tectonics of Western Tibet, between the Tarim and the Indus. Earth Planet. Sci. Lett. 142, 311–330.
Meert, J.G., 2003. A synopsis of events related to the assembly of eastern G(on)-8(r)0(e)-16.5(ladw

Song, S.G., Bi, H.Z., Yang, L.M., Qi, S.S., Li, W.F., Allen, M.B., Niu, Y.L., Su, L., 2018. HP-UHP Metamorphic Belt in the East Kunlun Orogen: Final Closure of the Proto-Tethys Ocean and Formation of the Pan-North-China Continent. J. Petrol. 59, 2043–2060.

Stern, R.J., Gerya, T., 2018. Subduction initiation in nature and models: A review. Tectonophysics 746, 173–198.

Stern, C.R., Kilian, R., 1996. Role of the subducted slab, mantle wedge and continental crust in the generation of adakites from the Andean Austral Volcanic Zone. Contrib. Mineral. Petrol. 123, 263–281.

Stern, R.J., Reagan, M., Ishizuka, Q., Ohara, Y., Whattam, S., 2012. To understand subduction initiation, study forearc crust: To understand forearc crust, study ophiolites. Lithosphere 4, 469–483.

Straub, S.M., Gomez-Tuena, A., Stuart, F.M., Zellmer, G.F., Espinasa-Perena, R., Cai, Y., Iizuka, Y., 2011. Formation of hybrid arc andesites beneath thick continental crust. Earth Planet. Sci. Lett. 303, 337–347.

Sun, S.S., McDonough, W.F., 1989. Chemical and isotopic systematics of oceanic basalts: implications for mantle composition and processes. Geol. Soc. Lond. Spec. Publ. 42, 313–345.

Sun, M., Long, X.P., Cai, K.D., Jiang, Y.D., Wang, B.Y., Yuan, C., Zhao, G.C., Xiao, W.J., Wu, F.Y., 2009. Early Paleozoic ridge subduction in the Chinese Altai: insight from the abrupt change in zircon Hf isotopic compositions. Sci. China. Ser. D Earth Sci. 52, 1345–1358.

Tatsumi, Y., 2001. Geochemical modeling of partial melting of subducting sediments and subsequent melt–mantle interaction: generation of high-Mg andesites in the Setouchi volcanic belt, southwest Japan. Geology 29, 323–326.

Tatsumi, Y., Suzuki, T., Kawabata, H., Sato, K., Miyazaki, T., Chang, Q., Takahashi, T., Tani, K., Shibata, T., Yoshikawa, M., 2006. The petrology and geochemistry of Oto-Zan composite lava flow on Shodo-Shima Island, SW Japan: remelting of a solidified high-Mg andesite magma. J. Petrol. 47, 595–629.

Thy, P., Beard, J.S., Lofgred, G., 1990. Experimental constraints on the origin of Icelandic rhyolites. J. Geol. 98, 417–421.

Tontini, F.C., Bassett, D., de Ronde, C.E., Timm, C., Wysoczanski, R., 2019. Early evolution of a young back-arc basin in the Havre Trough. Nat. Geosci. 12, 856–862.

van Hunen, J., Allen, M.B., 2011. Continental collision and slab break-off: A comparison of 3-D numerical models with observations. Earth Planet. Sci. Lett. 302, 27–37.

Wang, Q., Xu, J.F., Jian, P., Bao, Z.W., Zhao, Z.H., Li, C.F., Xiong, X.L., Ma, J.L., 2006. Petrogenesis of adakitic porphyries in an extensional tectonic setting, Dexing, South China: implications for the genesis of porphyry copper mineralization. J. Petrol. 47, 119–144.

Wang, Q., Wyman, D.A., Xu, J., Dong, Y., Vasconcelos, P.M., Pearson, N., Wan, Y., Dong, H., Li, C., Yu, Y., Zhu, T., Feng, X., Zhang, Q., Zi, F., Chu, Z., 2008. Eocene melting of subducting continental crust and early uplifting of central Tibet: evidence from central-western Qiangtang high-K calc-alkaline andesites, dacites and rhyolites. Earth Planet. Sci. Lett. 272, 158–171.

Wang, Q., Li, Z.X., Chung, S.L., Wyman, D.A., Sun, Y.L., Zhao, Z.H., Zhu, Y.T., Qiu, H.N., 2011. Late Triassic high-Mg andesite/dacite suites from northern Hohxil, North Tibet: eeochronology, geochemical characteristics, petrogenetic processes and tectonic implications. Lithos 126, 54–67.

Wang, M.J., Song, S.G., Niu, Y.L., Su, L., 2014. Post-collisional magmatism: Consequences of UHPM terrane exhumation and orogen collapse, N. Qaidam UHPM belt, NW China. Lithos 210, 181–198.

Wang, C.M., Tang, H.S., Zheng, Y., Dong, L.H., Li, J.H., Qu, X., 2019. Early Paleozoic magmatism and metallogeny related to Proto-Tethys subduction: insights from volcanic rocks in the northeastern Altyn Mountains, NW China. Gondwana Res. 75, 134–153.

Whalen, J.B., Currie, K.L., Chappell, B.W., 1987. A-type granites-geochemical characteristics, discrimination and petrogenesis. Contrib. Mineral. Petrol. 95, 407–419.

Windley, B.F., Alexeiev, D., Xiao, W.J., Kroner, A., Badarch, G., 2007. Tectonic models for accretion of the Central Asian Orogenic Belt. J. Geol. Soc. 164, 31–47.

Wu, J., Lan, C.L., Li, J.L., Yu, L.J., 2002. Geochemical evidence of MORB and OIB combination in Hongliugou ophiolite melanges, Altun fault belt. Acta Petrol. Mineral. 21, 24–30 (in Chinese with English abstract).

Wu, C.L., Yang, J.S., Robinson, P.T., Wooden, J.L., Mazdab, F.K., Gao, Y., Wu, S., Chen, Q., 2009. Geochemistry, age and tectonic significance of granitic rocks in north Altun, northwest China. Lithos 113, 423–436.

Xia, X.H., Song, S.G., Niu, Y.L., 2012. Tholeiite-Boninite terrane in the North Qilian suture zone: implications for subduction initiation and back-arc basin development. Chem. Geol. 328, 259–277.

Xinjiang BGMR, 1981. Geological Map of Shimiankuang, Xinjiang, China, Scale 1: 250000. Xinjiang Bureau of Geology and Mineral Resources (in Chinese).

Xinjiang BGMR, 2006. Geological Map of J46E006007 and J46E006008, Xinjiang, China, Scale 1: 50000. Xinjiang Bureau of Geology and Mineral Resources (in Chinese).

Xu, X., Song, S.G., Su, L., Li, Z.X., Niu, Y.L., Allen, M.B., 2015. The 600-580 Ma continental rift basalts in North Qilian Shan, northwest China: Links between the Qilian-Qaidam block and SE Australia, and the reconstruction of East Gondwana. Precambrian Res. 257, 47–64.

Yan, H., Long, X., Wang, X.C., Li, J., Wang, Q., Yuan, C., Sun, M., 2016. Middle Jurassic MORB-type gabbro, high-Mg diorite, calc-alkaline diorite and granodiorite in the Ando area, central Tibet: Evidence for a slab roll-back of the [Oc)29(m2(f)-2801-14.(s)-27